Synoptic Control of Convective Rainfall Rates and Cloud-to-Ground Lightning Frequencies in Warm-Season Mesoscale Convective Systems over North China

RUDI XIA

State Key Laboratory of Severe Weather, Chinese Academy of Meteorological Sciences, Beijing, China

DA-LIN ZHANG

State Key Laboratory of Severe Weather, Chinese Academy of Meteorological Sciences, Beijing, China,
and Department of Atmospheric and Oceanic Science, University of Maryland, College Park, College Park, Maryland

CUIHONG ZHANG

Key Laboratory of Meteorological Disaster/Pacific Typhoon Research Centre, Nanjing University of Information Sciences
and Technology, Nanjing, and Wuhan Central Meteorological Observatory, Wuhan, China

YONGQING WANG

Key Laboratory of Meteorological Disaster/Pacific Typhoon Research Centre, Nanjing University of
Information Sciences and Technology, Nanjing, China

(Manuscript received 5 July 2017, in final form 30 January 2018)

ABSTRACT

This study examines whether environmental conditions can control convective rainfall rates and cloud-to-ground (CG) lightning frequencies in mesoscale convective systems (MCSs) over north China (NC). A total of 60 identified MCSs over NC during June–August of 2008–13 were classified into 4 categories based on their high/low convective rainfall rates (HR/LR) and high/low CG lightning frequencies (HL/LL) (i.e., HRHL, HRLL, LRHL, and LRLL MCSs). MCSs with HR (HL) occurred most frequently in July (August), while those with LR or LL occurred most frequently in June; they followed closely seasonal changes. All MCSs were apt to form during afternoon hours. HRLL MCSs also formed during evening hours while HRHL MCSs could occur at any time of a day. A composite analysis of environmental conditions shows obvious differences and similarities among the HRHL, HRLL, and LRLL categories, while the LRHL MCSs exhibited little differences from the climatological mean because of its small sample size. Both the HRHL and HRLL MCSs occurred in the presence of upper-level anomalous divergence, a midlevel trough, and the lower-tropospheric southwesterly transport of tropical moist air. In contrast, LRLL MCSs took place as a result of daytime heating over mountainous regions, with little midlevel forcing over NC. The HRHL, HRLL, LRHL, and LRLL categories exhibited orders of the highest-to-smallest convective available potential energy and precipitable water but the smallest-to-largest convective inhibition and lifted indices. It is concluded that environmental conditions determine to some extent convective rainfall rates and CG lightning activity, although some other processes (e.g., cloud microphysics) also play certain roles, especially in CG lightning production.

1. Introduction

Mesoscale convective systems (MCSs), which are characterized by cold cloud tops of significant sizes and strength on satellite imageries and have various convective and stratiform rainfall structures on radar echoes, such as bow echoes and linear shaped (Jirak et al. 2003; Markowski and Richardson 2010), are a collection of thunderstorms that act as organized mesoscale weather systems. They are prolific producers of rainfall and cloud-to-ground (CG) lightning. For example, a single mesoscale convective complex (MCC; Maddox 1980) (i.e., a near-round-shaped MCS) can produce one-fourth of the mean annual CG lightning strikes at any site in the United States it passes over during the most intense phase of its life cycle (Goodman and MacGorman 1986). Similarly,

---

Corresponding author: Dr. Rudi Xia, xiard@cma.gov.cn

DOI: 10.1175/MWR-D-17-0172.1

MCSs can account for most of the warm season rainfall in much of the midwestern United States, and a group of MCSs occurring successively are very likely the most prolific producer of precipitation in the United States (Fritsch et al. 1986). In addition, rainfall and CG lightning have a close relationship (e.g., Cheze and Sauvageot 1997; Wu et al. 2017). Thus, in-depth understanding of the relationship between rainfall and CG lightning in MCSs and their favorable environments can help improve the related short-term forecasts.

The correlation coefficient r between convective rainfall and CG lightning, and the rain yields that are defined as the ratio of area-averaged convective rainfall amount to CG lightning flash count, have been generally used to quantify the relationship between convective rainfall and CG lightning in the Northern Hemispheric midlatitudes. Previous studies revealed that the value of r could range from 0.65 in a climatological study (Soriano et al. 2001) to 0.98 in a case study (Cheze and Sauvageot 1997). Similarly, the rain yields have a large range, too, but differ by regions (i.e., inland vs coastal regions, semiarid vs humid zones) because of different environments for convection. For example, rain yields varied from an averaged value of 6×10^7 kg flash^{-1} over the arid southwestern United States to 4×10^8 kg flash^{-1} over the tropical continent, and then to 10^{10} kg flash^{-1} in the tropical western Pacific Ocean (Petersen and Rutledge 1998). This variable may also increase from a mean value of 1.2×10^8 kg flash^{-1} for semiarid region to 2.1×10^8 kg flash^{-1} in humid region over the Iberian Peninsula (Soriano et al. 2001). Although a recent qualitative study (Xia et al. 2015) showed that convective rainfall has closer relationship to CG lightning than total rainfall, especially when a large proportion of stratiform rainfall is contained, the convective rain–CG lightning relationship is not simple, but highly nonlinear and complicated.

Numerous studies have been performed to study favorable environmental conditions for heavy rainfall production, such as an unstable atmospheric state with large convective available potential energy (CAPE), abundant moisture supply, and strong lifting (Tao 1980; Chen et al. 2004; Ricard et al. 2012; Zhang et al. 2013), with higher values of these parameters for heavier rain-producing MCSs. Some of these conditions have also been shown to play an important role in determining various CG lightning characteristics in thunderstorms. For example, based on a composite of 60 active and inactive CG lightning days during warm seasons, Mazarakis et al. (2008) found that high active CG lightning days in Greece were related to the presence of short-wave troughs at 500 hPa over the Ionian Sea and high values of absolute vorticity, equivalent potential temperature, and CAPE, whereas inactive CG lightning days were characterized with cold northwesterly flows at 500 hPa. Reap and MacGorman (1989) found that CG lightning flashes were strongly correlated with lower-level moisture fluxes and strong upward motion. Moreover, after analyzing nine distinct regions of severe storms during May–June 2002 over the central United States, Carey and Buffalo (2007) found that the relative high/low percentage of positive CG lightning in these storms was controlled by certain environmental conditions, such as moisture content in the lower to mid-troposphere, conditional instability, warm cloud depth, cloud-base height, and lower-level vertical wind shear. Lericos et al. (2002) showed that the location of a subtropical ridge relative to the Florida Peninsula affected the spatial and temporal distribution of CG lightning through the interaction of the associated environmental flows with coastal sea breezes over the Florida Peninsula. Sea- and land-breeze convergence zones have also been found by Reap (1994) to be favorable for high CG lightning activity.

Given a favorable synoptic-scale circulation with needed convective triggering, the development of thunderstorms would depend on whether or not atmospheric columns are conditionally unstable (i.e., with sufficient CAPE) since thunderstorms are convective in nature. In a climatological view, high CAPE, deep layer moisture, large warm cloud depth, and small negative lifted index (LI) tend to increase the occurrence rate of CG lightning flashes (Sheridan et al. 1997; Rudlosky and Fuelberg 2011). However, in some particular cases, relatively higher (lower) daily lightning counts may occur over relatively smaller (higher) CAPE environments (e.g., see Tapia et al. 1998).

The previous studies have shown obvious differences in synoptic-scale forcing (e.g., midlevel traveling disturbances, surface fronts) and atmospheric stability between raining/CG lightning and nonraining/CG lightning days, and in the dependence of dominant CG lightning polarity on synoptic forcing. However, rainfall amounts relative to CG lightning and their spatial distributions tend to have large variability from region to region and season to season. The nonlinear relationships between rainfall and CG lightning imply that the synoptic-scale environments favoring rainfall and lightning production may differ in the initiation and organization of thunderstorms and in the energy supply to thunderstorms. Moreover, various microphysical processes associated with both rainfall and lightning production may play important roles in determining the complicated phase transition of cloud hydrometeors including graupel and ice crystals that are important to lightning generation (Deierling et al. 2008).

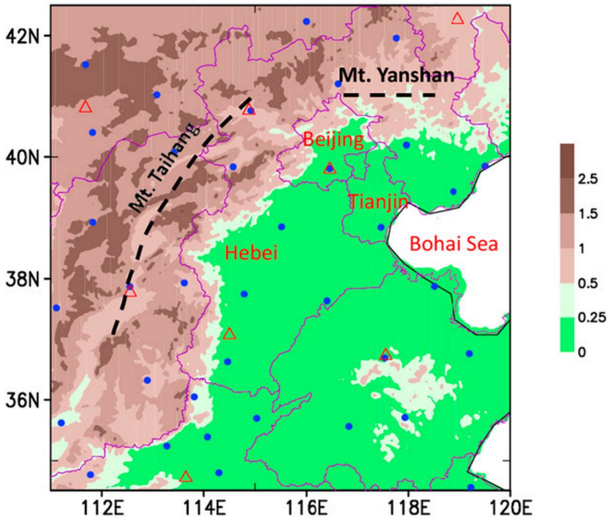

FIG. 1. The study domain of north China superimposed with CG lightning sensors (blue dots) and conventional upper-air stations (red triangles). Purple curved lines show provincial borders, with two cities, one province, and the Bohai Sea denoted in red. The shaded areas represent topography (km) with major mountains denoted in black and their ridges shown by dashed lines.

MCSs are responsible for many events of heavy rainfall (e.g., Zhang et al. 2013; Li et al. 2017) and frequent CG lightning (e.g., Liu et al. 2011) over north China (NC; 34.5°–42.5°N, 111°–120°E, see Fig. 1), where the capital circle of Beijing–Tianjian–Hebei is located. Heavy rainfall could produce large economic losses and casualties (e.g., Zhang et al. 2013) whereas moderate rainfall may significantly influence local transportation and urban drainage over NC. A 13-yr statistics study of Zhang et al. (2011) indicated that the lightning-induced annual damage rate per million people over Beijing ranks sixth among the 31 provinces in mainland China. Thus, it is highly desirable to explore some relationship between rainfall and CG lightning in MCSs, and understand the environments in which they develop, in order to help improve the regional weather forecasts of the associated rainfall and CG lightning events over NC.

During the past few years, considerable attention has been paid to studying MCSs occurring over NC in the context of climatology, composite, and case studies. These studies showed that MCSs over NC were apt to form over the western mountainous areas (see Fig. 1 for the terrain distribution), and then propagate eastward under the influence of midtropospheric westerly disturbances and lower-tropospheric southwesterly warm and moist air during summer months (Ding and Chan 2005; He and Zhang 2010; Chen et al. 2012; Xia et al. 2015). Sometimes new MCSs can be triggered by cold outflows produced by previously dissipated MCSs (e.g., Li et al. 2017). Heavy rain events, occurring most frequently in the months of June–August, were more associated with the following three types of synoptic-scale environments: a westerly propagating trough, a cold vortex, and a midlevel trough accompanied by a western Pacific subtropical high, which also accounted for the development of some other convective weather phenomena, such as gale-force winds, hail storms, and short-duration heavy rainfall (Su et al. 2011; Li et al. 2017). Some studies are dedicated to the lightning processes in MCSs over NC (e.g., Liu et al. 2011), but most of them were case studies, and few have examined MCSs with different rainfall and lightning characteristics, and the environmental control of those characteristics. In particular, little is known about the CG lightning frequency in heavy versus light rain-producing MCSs, and about their associated different environmental conditions, especially over NC.

Thus, the primary purpose of the present study is to investigate how statistically different rainfall and CG lightning characteristics of MCSs occurring over NC were, and what environmental parameters control those characteristics. Here, we hypothesize that certain environment conditions [e.g., CAPE and convective inhibition (CIN), dynamical lifting, lower-tropospheric dryness] determine more or less the relative convective rainfall amount and CG lightning activity of thunderstorms. Thus, one of the major objectives of this study is to test the above hypothesis by examining whether or not the synoptic circulations, in which thunderstorms are initiated and organized, could be classified into the following four rainfall–lightning categories of MCSs: high convective rainfall rates and high-frequency CG lightning flashes (HRHL), high convective rainfall rates but low-frequency CG lightning flashes (HRLL), low convective rainfall rates but high-frequency CG lightning flashes (LRHL), and the remaining low convective rainfall rates and low-frequency CG lightning flashes (LRLL), respectively. This objective will be achieved by analyzing observations of MCSs occurring over NC during the June–August months of 2008–13. Such a classification design is motivated by the observations that some precipitation particles in thunderstorms may be evaporated before falling into the ground (Bluestein and Parks 1983), and that heavy rainfall may occur in less convectively active conditions that are less favorable for lightning activity (Tapia et al. 1998). Note that it may be desirable to use total (i.e., CG + intracloud) lightning observations for the present study. Because of lacking intracloud lightning data, however, only CG lightning observations are used herein, like in most of the previous studies mentioned above.

The next section describes the data source used for the present study, and the methodology and algorithm used to classify the above four different rainfall–lightning categories. Section 3 shows to what extent the four categories could be classified, and then examines their temporal and spatial characteristics. A composite analysis of the different environmental conditions controlling the four categories of MCSs, and differences and similarities in CAPE, CIN, and other environmental parameters associated with the MCSs will also be presented. A summary and conclusions are given in the final section.

2. Data source and methodology

a. Data source

In this study, 0.1°-resolution hourly rainfall and brightness temperature of blackbody (TBB) data, CG lightning stroke data, and 12-hourly conventional upper-air observations over NC as well as 6-hourly ERA-Interim 0.75° × 0.75° resolution reanalysis data, from the European Centre for Medium-Range Weather Forecasts (ECMWF), during the months of June–August 2008–13 are used.

The 0.1°-resolution hourly rainfall data were derived by merging more than 30 000 rain gauge observations with the Climate Prediction Center morphing technique (CMORPH) satellite estimates through collaborations between the Chinese National Meteorological Information Center and the U.S. NOAA/Climate Prediction Center (e.g., Joyce et al. 2004; Xie and Xiong 2011; Pan et al. 2012; Shen et al. 2014). Shen et al. (2013) showed that the merged precipitation product is quite reasonable in terms of both the precipitation amount and spatial distribution. Moreover, the regional mean bias and root-mean-square error of the merged precipitation product decreased remarkably after quality control. Thus, the merged CMORPH and rain gauge data have been successfully used in many studies (e.g., to examine the diurnal cycle of precipitation) (Guo et al. 2016; Jiang et al. 2017).

The TBB data retrieved from the infrared channel of China's Fengyun geostationary meteorological *FY-2E/2C* satellite (Jin et al. 2010) are used herein to estimate the sizes of MCSs. The *FY-2C* was launched on 19 October 2004, and the *FY-2E*, which extends the service of *FY-2C*, was launched on 23 December 2008. The upgraded Stretched-Visible and Infrared Spin-Scan Radiometer (S-VISSR) is one of the major payloads on board the *FY-2C/2E*. This optical imaging radiometer consists of one visible channel and four infrared channels. The TBB products of both the *FY-2C* and *FY-2E*, with a 0.1° × 0.1° spatial resolution over the domain of 60°S–60°N, 45°–165°E, are provided once an hour and every 30 min for flood season. These data have been successfully used to study the morphology of MCSs over China (e.g., Yang et al. 2015).

The CG lightning stroke data was detected by ground-based Advanced Time of arrival and Direction system (ADTD) CG lightning detection sensors (see Fig. 1 for their distribution), which have been successfully used to study the climatology of CG lightning over the central and eastern portions of China, including NC (Xia et al. 2015), and to retrieve severe convective wind events (Yang et al. 2017). The CG lightning stroke data, providing the time of strokes on the order of millisecond and locations, are integrated to obtain hourly CG lightning flash data, with 0.1°-resolution, in order to have the same resolution as the hourly rainfall and TBB data for the convenience of studying their relationship. First, the positive ground strokes of less than 15 kA are removed in order to eliminate possible cloud discharge contaminations (Cummins and Murphy 2009). The strokes are then grouped to flashes by an algorithm developed by Cummins et al. (1998). The time and location of the first stroke are attributed to a flash, which may consist of a series of separate strokes that occurred during a 1-s time period within 10 km of the first stroke detected, with the time interval from the previous stroke of less than 0.5 s. As estimated by its manufacture, a single sensor has a detection efficiency of 90% and a location accuracy of about 500 m within a radius of 150 km. Xia et al. (2015) indicated that because of lacking adequate ground truth, the location errors of the detection network over NC can only be roughly estimated, with a value of about 2 km or less. This error would have little influence on our analyses, because the CG lightning flashes (on at least 300 grid cells according to the area criteria of MCSs, i.e., roughly 173 km × 173 km) are averaged over the coverage of cold cloud tops.

b. Definition of MCSs

Numerous studies have used satellite imageries to investigate various characteristics of MCSs (e.g., Jirak et al. 2003; Yang et al. 2015), which were mostly classified, following the work of Maddox (1980) who was the first to define MCCs—a particular round type of MCSs by both size (i.e., cloud shields with continuously low infrared temperature ≤ -32°C over an area $\geq 100\,000$ km^2 and interior cold cloud regions with infrared temperature ≤ -52°C over an area $\geq 50\,000$ km^2) and shape (i.e., eccentricity ≥ 0.7) thresholds. The −32°C size threshold was removed in some later works (e.g., Jirak et al. 2003; Yang et al. 2015) in order to simplify the identification procedure of MCCs, and the eccentricity threshold was adjusted for the purpose of investigating long-lived elongated MCSs. These long-lived systems were found to be the dominant satellite-defined MCSs (Anderson and Arritt 1998; Jirak et al. 2003), as they were the largest, most severe, and common rain-producing systems over the United States. Similarly, Yang et al. (2015) found that 80% of the MCSs occurring in China fell into an elongated category. Jirak et al. (2003) added another type of MCSs with smaller sizes (i.e., a cold cloud region $\leq -52°$C over an area $\geq 30\,000$ km^2, sometime reaching 50 000 km^2, referred to as β-scale MCSs), based on their finding that some MCSs having radar echoes of 100 km or more in length seemed to have cloud shields of at least 30 000 km^2 but less than 50 000 km^2. Their study indicates that the elongated β-scale MCSs were of higher-frequency events than those larger elongated MCSs.

Since the main purpose of this study is to explore the environmental control of both convective rainfall rate and CG lightning flash frequency of MCSs, we will adopt the philosophy of Jirak et al. (2003) by including those β-scale MCSs without considering shape and size differences (see Table 1). Nevertheless, this approach tends to exclude the early stages of some MCSs when their cloud shields have not reached 30 000 km^2. In addition, we require that each MCS to be included should have at least 1/2 of its area coverage and at least 2/3 of its life span both occurring within the study region (Fig. 1). On the other hand, if the MCS merged with any newly initiated clouds in its periphery or it split during its evolution within the study region, a larger one would follow but they were all considered as one MCS event since differentiating every cloud cell from the TBB data is almost impossible and also unnecessary. With the above approach, a total of 60 MCSs over NC during the warm seasons of 2008–13 are identified.

c. *Four categories of MCSs*

As mentioned earlier, we attempt to classify the MCSs into four categories in accordance with hourly rainfall rates and hourly CG lightning frequencies on $0.1° \times 0.1°$ grid cells. The hourly rainfall and CG lightning data are used herein partly due to the use of the 1-h period to resolve the life span of MCSs ranging from 5 to 11 h (to be shown in section 3a). The average rainfall rate of an MCS at a given hour, R_{1h}, is obtained from

$$R_{1h} = \frac{\sum\limits_{i,j=1}^{I,J} R_{i,j}}{N_R}, \tag{1}$$

where I and J are the total number of grid elements, along x and y directions, respectively, over an area including the MCS-associated rainfall and lightning; and $R_{i,j}$ and N_R are the hourly rainfall rates at individual grid elements that are equal or larger than 2.5 mm h^{-1} and the total number of the grid elements, respectively.

TABLE 1. Definition of MCSs by TBB satellite imagery.

Size	Cold cloud shields with continuous TBB $\leq -52°$C must have an area of $\geq 30\,000$ km^2, and their maximum size must be $\geq 50\,000$ km^2.
Duration	The size definition must be met for a period of ≥ 3 h.
Formation	The size definition is first satisfied.
Shape	Eccentricity (minor axis/major axis) ≥ 0.2 at the time of maximum extent.
Terminate	The size definition is no longer satisfied.

Because lightning activity is highly correlated to convective rainfall, a threshold rainfall rate of 2.5 mm h^{-1} is used to exclude the influence of stratiform rainfall, based on the work of Xu et al. (2014) who examined the relationship between stratiform rainfall rates from TRMM and brightness temperatures over the range of 25°–35°N in North America. In contrast, Houze (1993) indicated that convective rainfall rates in tropical MCSs are generally greater than 5 mm h^{-1}. Thus, a sensitivity test is conducted by comparing R_e using different threshold values (i.e., 2.5 and 5 mm h^{-1}). Results show that the 2.5 mm h^{-1} threshold is appropriate, because the correlation between R_e excluding rainfall rates $<$2.5 mm h^{-1} and R_e excluding rainfall rates $<$5 mm h^{-1} is almost linear, whereas the correlation between R_e excluding rainfall rates $<$2.5 mm h^{-1} and R_e including all of the rainfall rate greater than 0 is nonlinear. As a result, the average hourly rainfall rate of each MCS, R_e, is obtained by averaging R_{1h} over its life cycle to represent the system hourly rainfall rate. Similarly, the MCS CG lightning flash frequency L_e is obtained by averaging the mean hourly lightning frequency, L_{1h}, at each hour of the life span of an MCS:

$$L_{1h} = \frac{\sum\limits_{i,j=1}^{I,J} L_{i,j}}{N_L}, \tag{2}$$

where $L_{i,j}$ is the hourly CG lightning flash counts and N_L is the total number of grid elements with CG lightning flash counts higher than 0 flash over the same area as that used to estimate the hourly rainfall rates. Since rainfall/CG lightning occur mainly within and sometimes also near the periphery of cold cloud tops, the hourly rainfall/CG lightning distribution maps are checked to make sure that each calculated MCS region includes all of its associated rainfall/CG lightning.

The system-averaged values of R_e and L_e for all the 60 MCSs, which are 6.9 mm h^{-1} and 4.9 flashes h^{-1}, respectively, are then used as the two thresholds to classify them into the four different categories as mentioned above. That is, HRHL (20 cases), HRLL (14 cases), LRHL (6 cases), and LRLL (20 cases) MCSs, are determined by checking if R_e and L_e for each MCS are higher or lower than the threshold values of 6.9 mm h^{-1} and 4.9 flashes h^{-1}, respectively. Note that the relationships between the MCSs sizes and the magnitudes of R_e and L_e are not linear. Namely, small-sized MCSs may produce either high or low R_e/L_e, and large-sized MCSs were apt to produce moderate R_e/L_e. Note also that the small sample size for LRHL MCSs implies the low occurrence rate of LRHL events in MCSs; the related causes will be discussed in section 3b.

Figure 2 shows scatterplots of R_e and L_e associated with the 60 MCSs with respect to the thresholds. One may note a few interfacing points that do not appear to deviate markedly. In our opinion, requiring large deviations among them does not seem to be realistic because R_e and L_e from all the MCSs over a region must be continuous in their distributions. Moreover, a series of sensitivity experiments has been conducted by including or excluding the interfacing points (not shown). Results show little impact on the composite circulations of each category to be shown later. In addition, 52 MCSs would fall into the same category when the maximum hourly rainfall/CG lightning rates at a given hour (not shown), instead of the area-averaged hourly rainfall/CG lightning rates, are used to calculate R_e and L_e, respectively. This illustrates further that the designed methodology represents well the highest rainfall/CG lightning intensity of MCSs.

One may also note that each category contains a couple of outliers at their higher ends. They appear to be reasonable since extreme rainfall or lightning events are generally of very low probability. For example, the rightmost HRLL MCS (i.e., with R_e = 11.21 mm h^{-1}, and L_e = 4.56 flashes h^{-1}) occurred on 26 July 2012 under the influence of a subtropical high and the extratropical transition of Typhoon Vicente in south China with ample water vapor in the lower-level southwesterly flows to the east, and a deep midlevel trough to the west. Its peak daily rainfall amount of 345 mm was observed at Tianjin (see its location in Fig. 1). An opposite extreme in lightning is an HRHL event, located at the central top (i.e., R_e = 7.91 mm h^{-1}, and L_e = 20.22 flashes h^{-1}), which occurred in the middle portion of NC on 16 August 2013, when an MCS developed ahead of a cold front extending southward through NC (not shown). Morning soundings (0800 LST) taken at Beijing and Xingtai, Hebei Province (see its location in Fig. 1), exhibited CAPE values of about 1230 and 2825 J, respectively. Similarly, the rightmost extreme HRHL MCS occurring on 8 August 2010 (i.e., with R_e = 12.38 mm h^{-1}, and L_e = 8.25 flashes h^{-1}) was influenced by a midlevel trough and a spilt subtropical high caused by Typhoon Dianmu in the northwest Pacific.

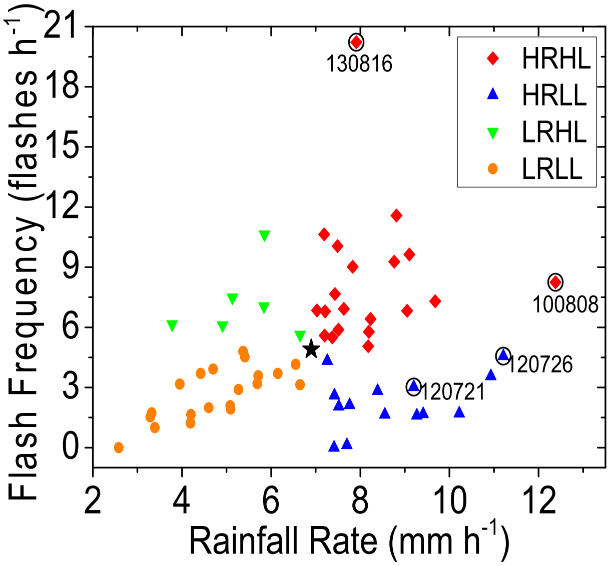

FIG. 2. Scatterplots of the life-span-averaged CG lightning flash frequency (L_e, flashes h^{-1}) vs the life-span-averaged rainfall rates (R_e, mm h^{-1}) for 20 HRHL (red), 14 HRLL (blue), 6 LRHL (green), and 20 LRLL (orange) MCS events over NC during the June–August months of 2008–13. The symbol "★" shows the position of the system-averaged R_e and L_e for the 60 MCSs (see text). A few extreme events mentioned in the text are highlighted with black hollow circles and dates in forms of yymmdd.

Note that the system-averaged rainfall rates or lightning frequencies (i.e., R_e or L_e) may make some extreme events to be "nonextreme" ones after smoothing out the associated local extreme values in cases of widespread rainfall or lightning, because of relatively large values in the denominator of Eq. (1) or (2). One example was the HRLL event occurring in Beijing and its adjacent area on 21 July 2012 (Zhang et al. 2013; Zhong et al. 2015), which has an R_e value of 9.2 mm h^{-1}, but with a record-breaking local rainfall amount of 460 mm in 19 h. On the other hand, a small coverage of rainfall or lightning may result in a high value of R_e or L_e when some grid elements exhibited high rainfall rates or lightning frequencies, like the above-mentioned two HRHL events at their high ends.

In summary, we may state that despite the above limitations, the four categories of MCSs, so classified in accordance with their above- or below-averaged values of R_e and L_e (Fig. 2), are indeed encouraging because they demonstrate the rationality of our hypothesis and the robustness of the classifying algorithm so designed. This result will allow us to perform composite analyses of the spatiotemporal characteristics and environmental conditions associated with the four different categories of MCSs in the next section.

d. Composite of synoptic circulations

The composite of synoptic circulations from the lower to upper troposphere close to the initiating time for each

TABLE 2. Summary of the environmental thermodynamic parameters associated with the development of various categories of MCSs.

Index	Description
Surface-based convective available potential energy (SBCAPE; J)	$\mathrm{SBCAPE} = \int_{\mathrm{p1}}^{\mathrm{p2}} R_d(T_v' - T_v)\, d\ln p$, where p1 and p2 are the pressure at the level of free convection and equilibrium, respectively, for an air parcel originating at the surface; R_d is specific constant for dry air; and T_v' and T_v are the virtual temperature of air parcel and the environment, respectively.
Most unstable CAPE (MUCAPE; J)	As for SBCAPE, but for the most unstable air parcel in the lowest 300-hPa layer.
Convective inhibition (CIN; J)	As for CAPE, but that p1 and p2 are the pressure at the surface and free convection level, respectively.
Lifted index (LI; °C)	$\mathrm{LI} = T_{500} - T_{500}'$, where T_{500}' is the temperature of a parcel lifted from the surface dry adiabatically to the saturation point and then moist adiabatically to 500 hPa.
Precipitable water (PW; mm)	$\mathrm{PW} = 1/g \int_{\mathrm{p1}}^{\mathrm{p2}} q\, dp$, where p1 and p2 is pressure at the surface and 100 hPa, respectively, and q denotes the mixing ratio of water vapor.

category are examined using the ERA-Interim data to see if there is any distinct difference in larger-scale forcings that could distinguish between the four different categories of MCSs. (We believe that the 6-h temporal resolution of the ERA-Interim data should be sufficient to resolve significant changes in synoptic-scale flows.) To do so, the mean circulation of the samples in each category will be evaluated for statistical significance using one sample Student's *t* test (Wilks 2011). Areas with the significance level at 95% and larger imply that the mean circulation of the samples differs significantly from the climatological mean field that is the averaged one during the June–August months of 2008–13 in this study. Note that the small sample size for LRHL MCSs may affect the significance of composite results.

e. *Sounding-derived parameters*

After discussing different favorable environmental circulations, it is desirable to examine statistically their associated conditional instability consisting of CAPE, CIN, and convective lifting as well as the other environmental factors (Moncrieff and Miller 1976; Colby 1984; see Table 2). The potential for convective development is usually measured by CAPE, which is the vertically integrated thermal buoyancy from the level of free convection to equilibrium level, while the energy needed to lift a parcel from the surface to the level of free convection is measured by CIN. Two types of CAPE, including the surface-based CAPE (SBCAPE; i.e., for an air parcel originating from the surface layer) and the most unstable CAPE (MUCAPE; i.e., for the most unstable air parcel in the lowest 300 hPa layers), are examined, respectively. The virtual temperature is used herein to calculate both SBCAPE and MUCAPE because ignoring the virtual correction may have substantial influence for MCSs with small CAPE (Doswell and Rasmussen 1994). If CAPE is equal to 0, CIN is meaningless and will be discarded. This condition may occur often in weak convective storms (e.g., LRLL MCSs). The LI (Galway 1956), representing the potential of convective lifting at 500 hPa, is the temperature difference between an air parcel lifted adiabatically and its environment at that level. A negative LI indicates that the air parcel can keep moving upward because of positive buoyancy. The water vapor supply condition is measured by precipitable water (PW) integrated from the surface to 100 hPa. Sounding stations closest to the MCSs at the time prior to their formations are selected for composite analyses. If there was any preexisting MCS over the target region, the sounding closest to the formation time is selected, which only occurs to one HRHL MCS.

In order for the results obtained to be meaningful, the differences between each pair of the above-mentioned four categories have to be statistically significant. That is, the samples of each category are first checked for normalized distribution at the 95% significant level, and then, a two-sample *t* test is performed to test the null hypothesis that the difference between two independent sample means is zero. If one category for a given parameter is found to be nonnormal, then the nonparametric Wilcoxon–Mann–Whitney test is applied to the associated pair (Wilks 2011), since this methodology does not require an assumed normal distribution.

3. Results

In this section, we examine the different temporal (i.e., from monthly to diurnal) and spatial characteristics

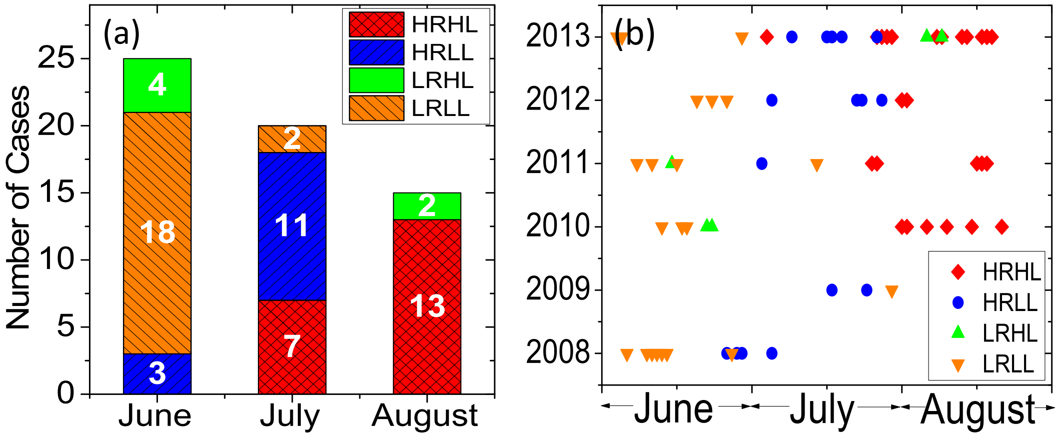

FIG. 3. Monthly distribution of (a) the total number of the HRHL (red), HRLL (blue), LRHL (green), and LRLL (orange) MCSs occurring over NC; and (b) each category of MCSs in each year, during the June–August months of 2008–13.

among the four categories of MCSs, followed by the composite of their associated larger-scale circulations, and the environmental thermodynamic conditions for their development.

a. Temporal and spatial characteristics

It is apparent from Fig. 3a that the number of MCSs, as defined herein, decreased gradually from 25 in June to 20 in July and 15 in August. This was consistent with the finding of Chen et al. (2012) that MCSs over NC occurred most frequently in June, and least frequently in August, based on radar mosaic climatology, but it differed from that of Yang et al. (2015) who found a slight higher frequency of MCSs in July than that in June. The latter may be attributed to their inclusion of short-duration MCSs (i.e., 1–2 h) with a larger study region than the present one. In contrast, the monthly variation of each category of MCSs differed significantly from that of the total MCS population. Figure 3a also shows that the LRLL category was most frequent in June (18 cases), and then decreased dramatically in July (2 cases) and disappeared completely in August, accounting for 72%, 10%, and 0% of the total MCSs in its corresponding month, respectively. This implies that MCSs over NC were the least prolific in CG lightning and rainfall during June. By comparison, the HRLL category increased markedly from June (3 cases) to July (11 cases), while the HRHL cases in August (13 cases) nearly doubled that in July (7 cases). The increased high-rainfall MCSs (i.e., under HRLL and HRHL) toward the month of August are consistent with both the increased surface air temperature, and the moister monsoonal air of tropical origin during this period (Tao 1980), namely, associated with seasonal changes. In particular, high rainfall cases occurred most frequently in July (18 cases) and then August (13 cases), which were more closely related to the typical warm and moist airstreams associated with the South China Sea summer monsoon (Ding and Chan 2005). Similarly, high CG lightning MCSs were most frequent (totally 15) in August, a month in which conditional instability was on average the highest due to the presence of the strongest surface heating of a year. This is in agreement with the results of Xia et al. (2015) and Wu et al. (2016). There were only six LRHL cases during the warm season, four of which occurred in June, which is typically a dry month in NC, indicating that MCSs with low rainfall rates are also the least prolific in CG lightning production.

Figure 3b shows significant annual variability of the four categories of MCSs from 2008 to 2013. That is, the LRLL MCSs occurred most frequently in 2008, whereas the HRHL MCSs occurred more frequently in 2010 and 2013 than those in the other years. It is of interest that the same category of MCSs was apt to occur continuously, implying that short-term climatic conditions and larger-scale environments may play some roles in determining how much rainfall and lightning in MCSs would be produced by providing similar background conditions.

Figure 4 shows what periods (at 6-hourly intervals) of a day (i.e., LST = UTC + 8 h) the four categories of MCSs formed. Note that the storm formation time implied herein is not the hour at which the associated cloudiness was first seen, but the hour at which the size criteria of an MCS (Table 1) were first met. Results show that all of the four types of MCSs were apt to form in the afternoon, which coincided with the timing of the peak CG lightning and rainfall rates found by Xia et al. (2015) and of high storm frequencies found by Chen et al. (2012). This implies that these systems were highly

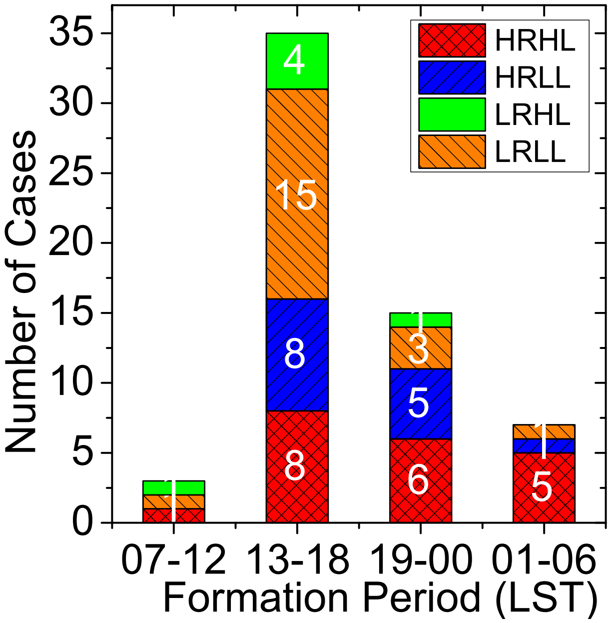

FIG. 4. Diurnal distribution of the HRHL (red), HRLL (blue), LRHL (green), and LRLL (orange) MCSs formed as a function of LST at 6-hourly intervals.

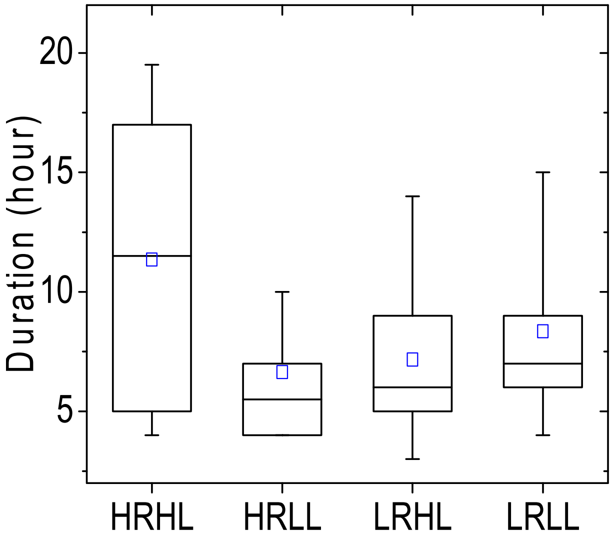

FIG. 5. Box-and-whisker plots of the duration of the HRHL, HRLL, LRHL, and LRLL MCSs. Boxes, whiskers, and blue squares show their individual interquartile ranges, 90th and 10th percentile, and the mean value, respectively.

related to conditional instability caused by solar heating. The HRHL MCSs could form at any time period, and this was also true for the LRLL MCSs. It follows that MCSs formed in the afternoon and evening hours can be any category, whereas those that formed in the early morning hours were mostly the HRHL MCSs.

Figure 5 shows that the durations of the four categories of MCSs spanned in the ranges of 5–17, 4–7, 5–9, and 6–9 h for the HRHL, HRLL, LRHL, and LRLL MCSs, respectively, with the averaged values of 11.4, 6.6, 7.2, and 8.4 h. They give a mean duration of about 8.8 h for the 60 MCSs, which is longer than that of 7.4 h over China as indicated by Yang et al. (2015). Again, this difference appears to be attributable to their inclusion of shorter-duration (1–2 h) MCSs. Clearly, the HRHL MCSs were on average longer lived, whereas the HRLL MCSs were short lived, with 70% of them lasting for less than 6 h. It should be mentioned that most of the long-lived MCSs had experienced the merging processes with other convective elements, especially for those whose life spans could reach as long as 28 h. In addition, these longer-lived MCS appeared to benefit from persistent favorable larger-scale forcings. For example, the two successive long-lived HRHL MCSs (i.e., that lasted for 20 and 16 h, respectively), which caused one casualty and great economic losses in NC (Rainstorm Yearbook, http://www.whihr.com.cn/) on 14–16 August 2011, were influenced by the passage of a cold front with a lower-tropospheric vortex.

Figure 6 shows the spatial characteristics of the four categories of MCSs, as indicated by tracking the evolution of their associated coldest cloud tops. Except for LRHL MCSs, which are the least frequent, the other three categories of MCSs present apparent preferences. The HRHL and HRLL MCSs dominated the plain areas to the east of Mt. Taihang, the southwest of Mt. Taihang, and the northeast of Mt. Yanshan (Figs. 6a,b), where southwesterly moist and warm airstreams often prevailed during the summer months (He and Zhang 2010). In contrast, the LRLL MCSs occurred mainly over the northern mountainous region (Fig. 6d), indicating clearly the importance of topographical lifting of Mt. Taihang and solar heating in the initiation of these thunderstorms mostly during the afternoon hours. The topographical lifting could also account for about half of the HRHL cases occurring over the western or close to the foothill of the western mountains (Fig. 6a). In agreement with the studies of He and Zhang (2010) and Chen et al. (2012), most of the MCSs analyzed herein tended to have an eastward displacement tendency. However, some other MCSs are found to move very differently from the mean state (e.g., southward or northwestward) partly because of the effects of convective splitting and merging that also influenced the life spans of the MCSs, and partly because of the interaction of convective development with larger-scale flows.

b. *Composite synoptic-scale circulations*

After seeing the distinct spatiotemporal characteristics of the four categories of MCSs, we may assume

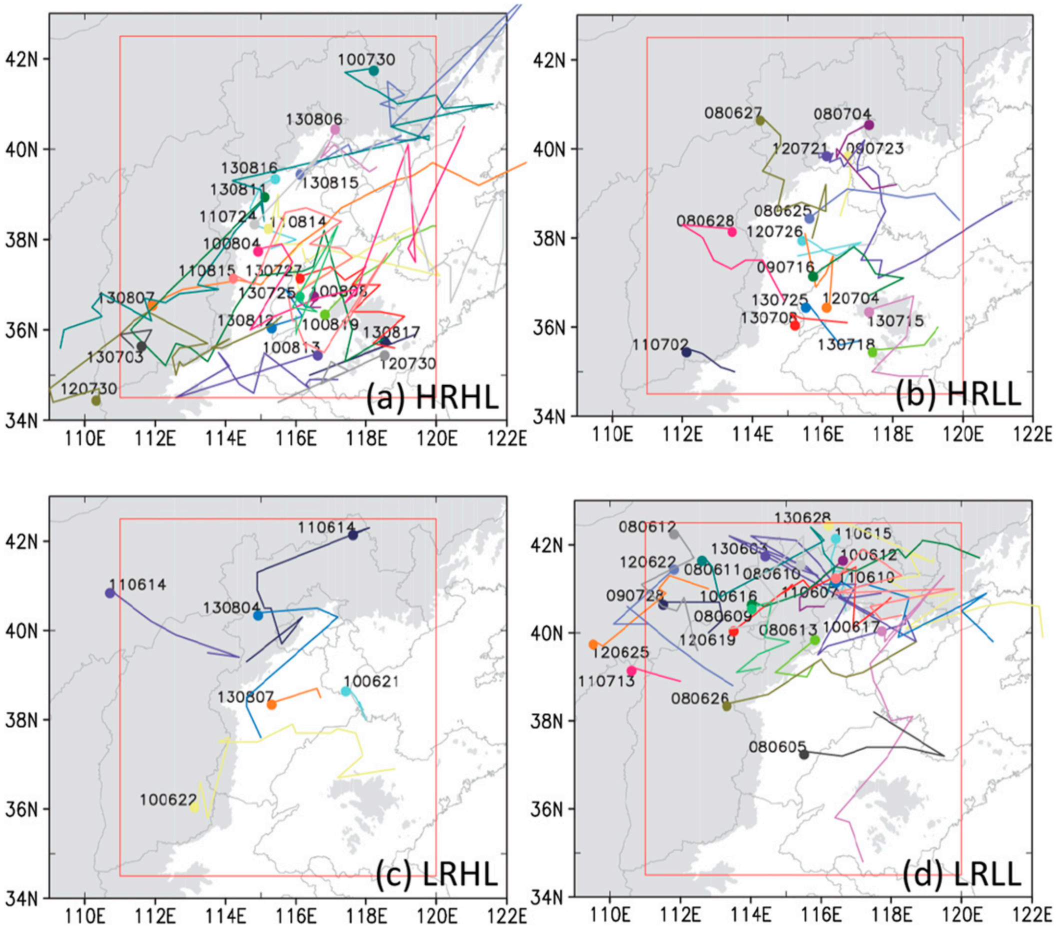

FIG. 6. Tracks of the (a) HRHL, (b) HRLL, (c) LRHL, and (d) LRLL MCSs as indicated by the coldest cloud-top locations. Solid dots represent the locations of the coldest cloud top at the formation time, and the numbers close to the dots denote the associated dates (yymmdd). The gray shaded area represents terrain height higher than 250 m.

significantly different synoptic-scale circulations, especially those associated with seasonal changes were responsible for generating these distinct characteristics. For this purpose, we analyze the composite of synoptic circulations at 850-, 700-, 500-, and 200-hPa levels at or near the formation time for each category of MCS events. Figure 7 shows such a composite for the HRHL MCSs. At 200 hPa, the study area was situated on the south of the upper-level jet streams with divergent wind anomalies, which was favorable for upward motions (Fig. 7a). (Note that all the anomalies are obtained with respect to their corresponding fields that are averaged during June–August of 2008–13, which are also referred to herein as the climatological mean flows.) At 500 hPa, the study area was located ahead of a trough axis, with a negative and a positive height anomaly on the northwest and southeast, respectively (Fig. 7b). Meanwhile, we see an abnormally strong subtropical high over the northwest Pacific with its ridge axis extending to about 115°E. All these imply that warm and moist monsoonal air could be readily transported to the study region by southwesterly winds on the northwest side of the subtropical high, while experiencing quasigeostrophic (QG) lifting ahead of the trough axis during its course to NC. This result is consistent with the occurrences of all the HRHL events in July and August (Fig. 3a), in which months the subtropical high (summer monsoon) reaches NC. We also see the distribution of northerly winds on the northwest of NC, which would presumably transport drier and colder air masses to the study area. The 500-hPa trough also suggests the presence of cold fronts in assisting in the initiation and developing of deep convection. This was indeed true at 700 hPa (Fig. 7c), showing southwesterly wind anomalies from the South China Sea to the study region. An analysis of the surface maps provided by Chinese National Meteorological Center indicates that cold fronts were present in three quarters of the HRHL events (not shown). The 850-hPa map does show the

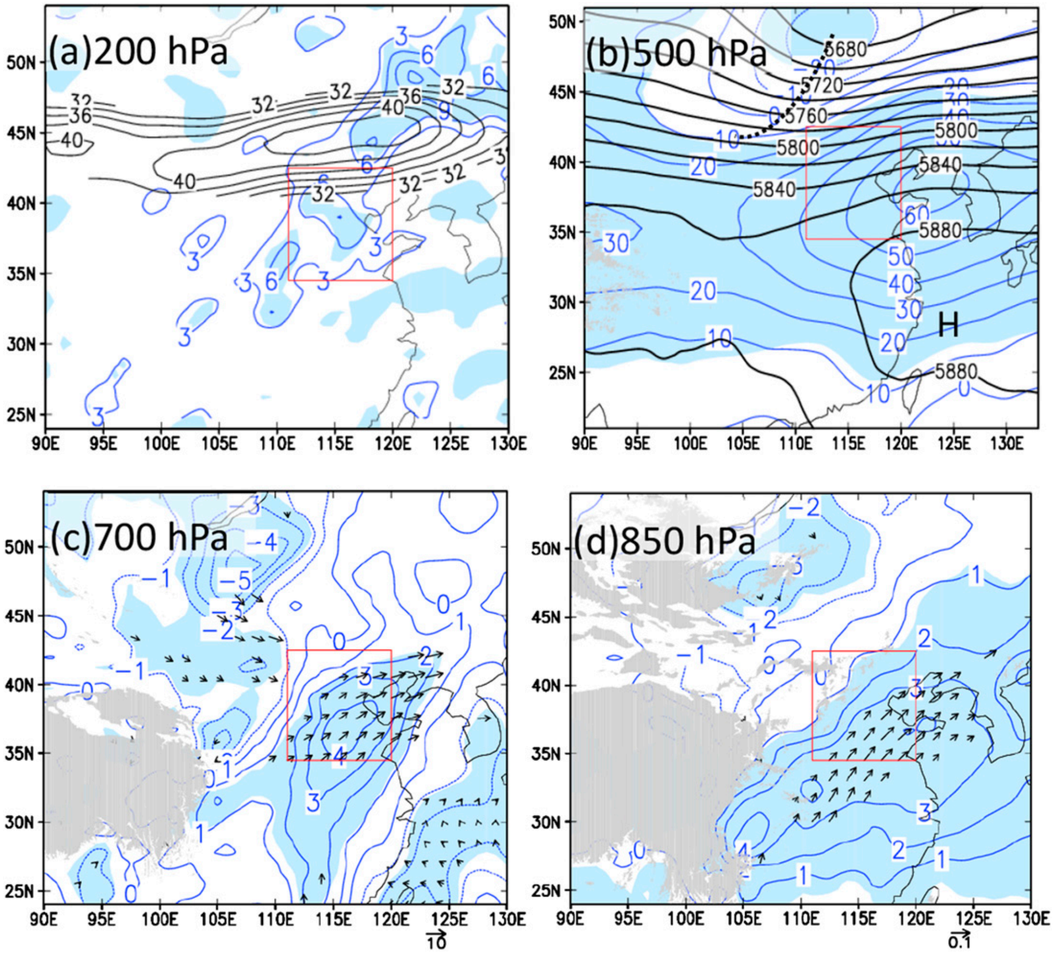

FIG. 7. Composite of the synoptic-scale circulations at or close to the formation hour of the HRHL MCSs. (a) Divergence anomalies (blue contoured at $3 \times 10^{-5}\,\mathrm{s}^{-1}$ intervals), and horizontal velocities greater than $30\,\mathrm{m\,s^{-1}}$ (black contoured at $2\,\mathrm{m\,s^{-1}}$ intervals) at 200 hPa. Note that only horizontal velocities having the statistical significance at 95% confidence level are shown. (b) Geopotential height (black contoured at 20-gpm intervals), and its anomalies (blue contoured at 10-gpm intervals) at 500 hPa. Dotted lines represent the trough axis. (c) Meridional wind speed anomalies (blue contoured at $1\,\mathrm{m\,s^{-1}}$ intervals) at 700 hPa. Vectors denote horizontal winds ($\mathrm{m\,s^{-1}}$, the speed scale is given beneath the bottom right of the panel) having the statistical significance of 95% confidence level. (d) Temperature anomalies (blue contoured at 1-K intervals) at 850 hPa. Blue shadings denote the areas of the associated anomaly field with the statistical significance at 95% confidence level. Vectors denote water vapor flux vectors ($\mathrm{kg\,kg^{-1}\,m\,s^{-1}}$, the scale is given beneath the bottom right of the panel) having the statistical significance at the 95% confidence level. Gray shadings in (c) and (d) represent terrain. The letter "H" denotes the western Pacific subtropical high. The red rectangle represents the study area of north China as shown in Fig. 1.

presence of positive (negative) temperature anomalies in the southwesterly (northerly) flows (Fig. 7d), confirming the above analysis. Since the above anomaly fields all pass the statistical significance tests at above 95% level over large areas, as indicated by blue shadings, we may state that the upper-tropospheric divergence, and the southwesterly warm and moist air meeting with the northwesterly dry and cold air in the lower troposphere played important roles in providing favorable conditions for the development of the HRHL events over NC.

Figures 8a and 8b show the selected south–north and west–east vertical cross sections through the MCSs region, respectively. We see the transport of high pseudo equivalent potential temperature (θ_{ep}) air originating from the South China Sea (Fig. 8a), accounting for the presence of potential instability over NC, as indicated by vertical decreases in θ_{ep} in the lowest 600 hPa. In fact, the lower-tropospheric θ_{ep} values over the plain area in the study region were higher than those at the same latitude and altitude (Fig. 8b). In addition, a cold front

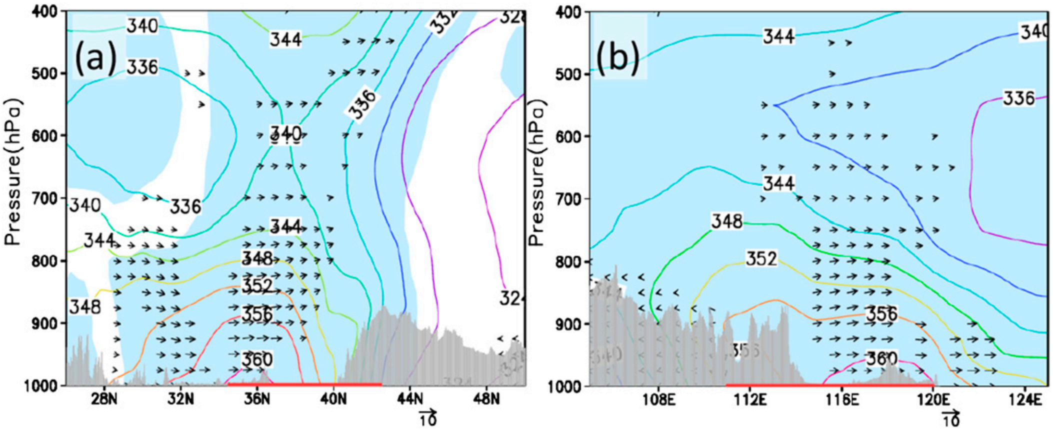

FIG. 8. Vertical cross sections of in-plane flow vectors composited by (a) meridional wind (m s^{-1}) and vertical motion (cm s^{-1}); and (b) zonal wind (m s^{-1}) and vertical motion (cm s^{-1}); with the statistical significance at and above the 95% confidence level (shaded) for pseudoequivalent potential temperature θ_{ep} (contoured at 4-K intervals) at or most close to the formation hour for the HRHL MCSs. They are taken from the south to north along (a) 117°E and (b) from the west to east along 36°N (see Fig. 7). Gray areas represent terrain. The bolded red color on the horizontal axis denotes the study area of NC. Note that the typical characteristics of cross sections through other latitudes or longitudes of the studied region were similar to those shown in this figure.

could be seen from the large horizontal gradients in θ_{ep} in the south–north cross section (Fig. 8a).

By comparison, the synoptic conditions associated with the HRLL MCSs were similar in most aspects to those of the HRHL MCSs, but with some distinct differences. Like the synoptic circulations associated with the HRHL events, Fig. 9 shows the presence of a positive divergence anomaly (Fig. 9a), and a midlevel weak trough over NC with a well-defined subtropical high to the southeast (Figs. 9b,c), a warm (and moist) southwesterly flow meeting with a cold (and dry) northwesterly flow over NC (Fig. 9c). Primary differences between the HRLL and HRHL MCSs were more related to the amplitudes and locations of the above anomaly fields; that is, a stronger divergence anomaly at 200 hPa but without the upper-level jet stream effect (cf. Figs. 9a and 7a), the southeastward placement of a weaker trough and the slight southwestward placement of the subtropical high at 500 hPa (cf. Figs. 9b and 7b), and the southeastward placement of the southwesterly warm (and moist) current and the northerly cold (and dry) current anomalies at 700 hPa (cf. Figs. 9c and 7c). Although the weaker midlevel trough, shown in Fig. 9b, did not differ significantly from the climatological mean flow (not shown), it was the subtropical high that played an important role in determining the location of heavy rainfall from the HRLL MCSs (Chen et al. 2004). The frontogenesis process over NC was relatively weaker than that in the HRHL events, as indicated by the weaker anomalies of temperature gradients at 850 hPa (Fig. 9d) and of θ_{ep} gradients (Fig. 10a).

Vertical cross sections also show the presence of potential instability associated with the transport of high-θ_{ep} air from the South China Sea by southwesterly flows in the lower troposphere, but the potential instability of the study region was weaker than that of HRHL (cf. Figs. 10a and 8a). Similarly, Fig. 10b shows the presence of much weaker potential instability in the west–east cross section through the study region. The vertical lapse rate of θ_{ep} from the planetary boundary layer (PBL) to 700 hPa was about 8 K (i.e., from 348 to 340 K) for the HRLL MCSs (Fig. 10b), as compared to 16 K (i.e., from 360 to 344 K) for the HRHL MCSs (Fig. 8b), and nearly the same magnitude of the θ_{ep} differences also occurred in the lower troposphere (cf. Figs. 10a and 8a). The smaller value of $|\partial\theta_{ep}/\partial z|$ illustrates relatively weaker conditional instability of the atmosphere, which helps partly explain why much less CG lightning activity occurred in the HRLL MCSs than that in the HRHL MCSs.

In contrast to the above two categories of MCSs (i.e., HRHL and HRLL), the LRLL events exhibited several different synoptic environmental conditions. Figure 11 shows favorable synoptic conditions for convective development in the lower reach of the Yangtze River and south China, such as an upper-level jet with strong right-side divergence, a 500-hPa trough increasing in amplitude southward, and pronounced anomalies in lateral wind shear in the lower troposphere. However, over NC, there was a weak ridge in the midtroposphere, a smaller area coverage of a weaker divergence anomaly at the upper levels, a weaker anomaly in southerly winds at

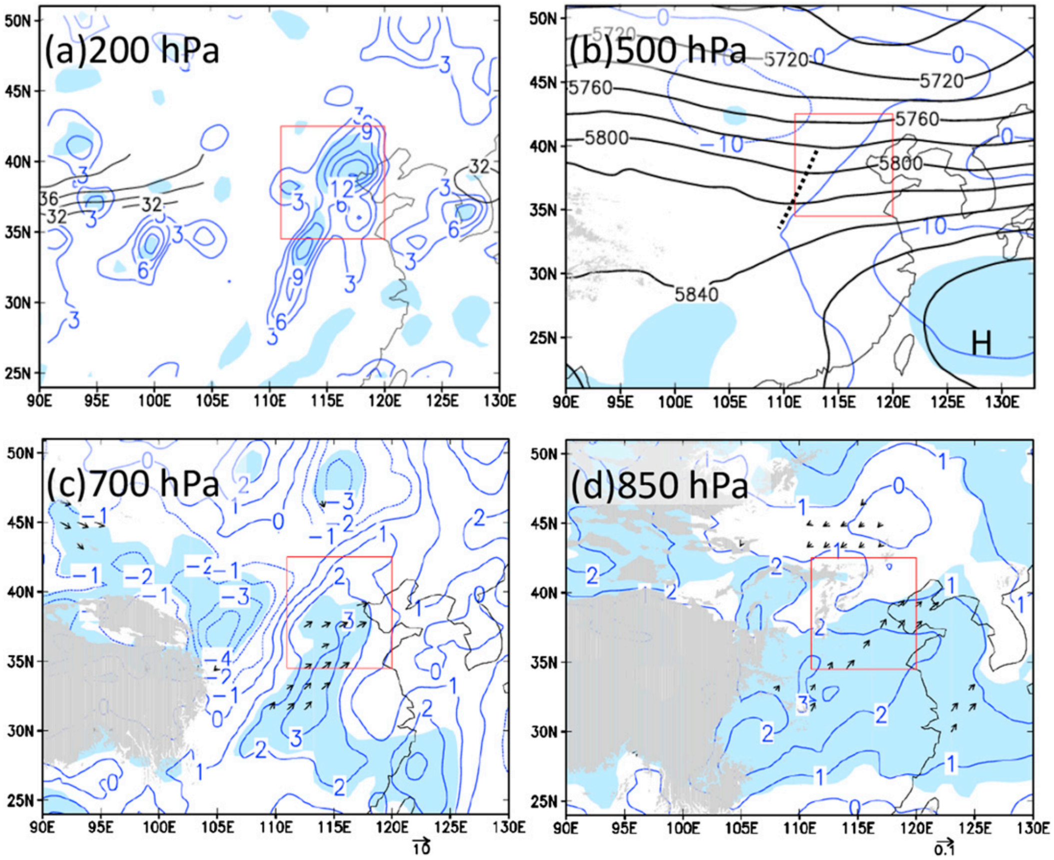

FIG. 9. As in Fig. 7, but for the HRLL MCSs.

700 hPa on the north of NC, and an inversed temperature variation at 850 hPa over NC compared to those associated with the HRHL MCSs (cf. Figs. 11d and 7d). All these indicate the presence of weak QG forcing for MCS development. As conjectured earlier, the initiation of the LRLL MCSs may be attributed to the afternoon heating over the mountainous area, as indicated by warm anomalies over the mountainous region at 850 hPa (Fig. 11d) and the surface (not shown) and the presence of potential instability in Fig. 12b. However, unlike the HRHL and HRLL MCSs, the rainfall rates are low because of lacking abundant water vapor transported from

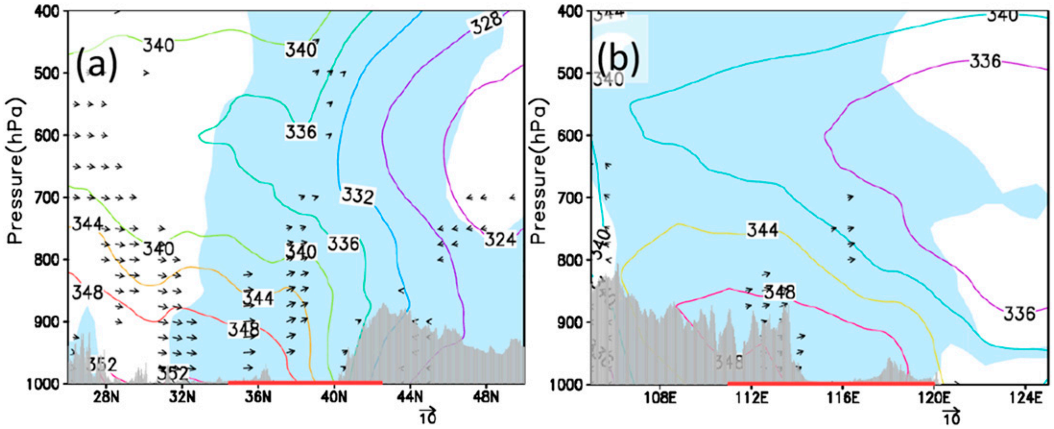

FIG. 10. As in Fig. 8, but for the HRLLMCSs.

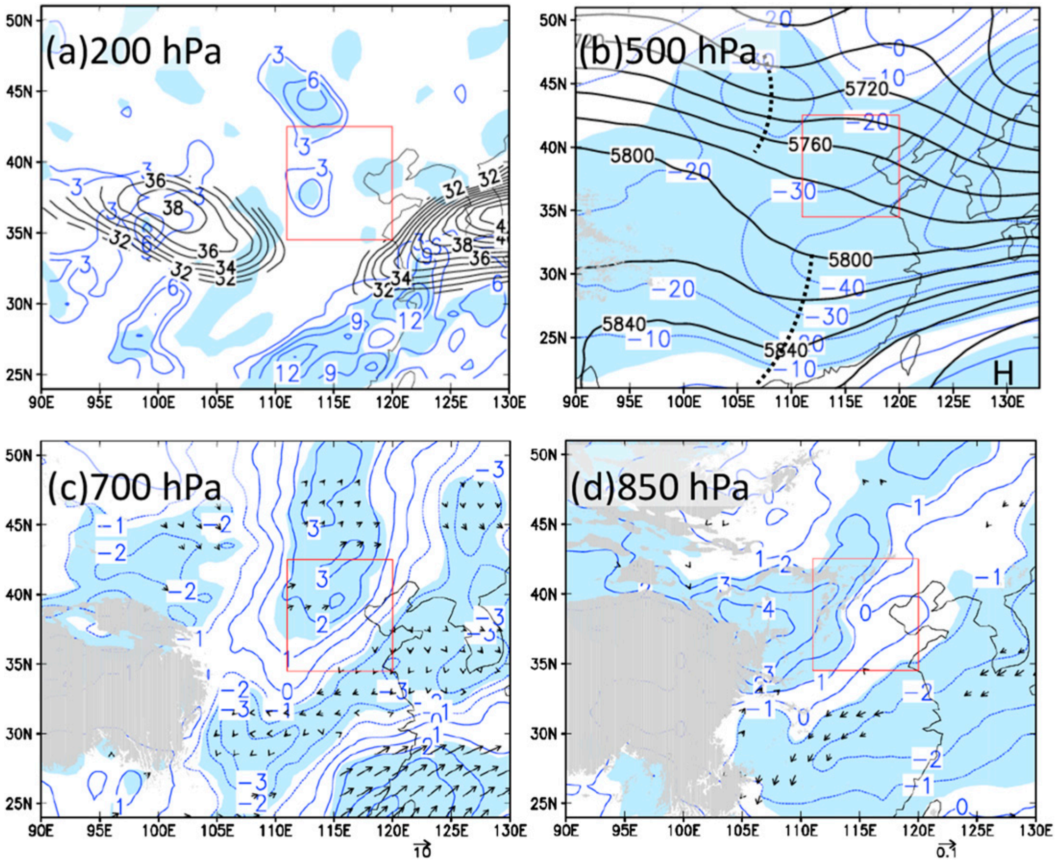

FIG. 11. As in Fig. 7, but for the LRLL MCSs.

the South China Sea (Figs. 11c,d). This result is consistent with the occurrences of most LRLL events in June (Fig. 3a), in which month the subtropical high stays in south China. This can also be seen from the presence of little potential instability to the south of 40°N and east of 119°E and the absence of any LRLL MCS over NC (cf. Figs. 12a,b and 6c). All the differences were consistent with the monthly variations of the subtropical high and solar heating as well as the northward placement of the LRLL MCSs relative to that of the HRHL and HRLL events.

The composite synoptic-scale conditions for the LRHL MCSs are not shown because of their small sample size (i.e., only six) and the lack of significance regions compared with the climatological mean field. For the sake of completeness, however, we provide briefly their associated environmental conditions as follows. NC was located between a ridge on the west and a closed low on the northeast without any significant anomaly from the climatological mean, implying the presence of little favorable QG lifting. In addition, much less moisture supply from the lower latitudes could reach NC, where the atmospheric environment is relatively dry. As a result, rainfall intensity would be substantially reduced, as expected. On the other hand, as compared to the LRLL MCSs, the low-level heating anomaly over and to the west of NC was relatively higher, which could account for the triggering of LRHL MCSs during the afternoon period over the mountainous regions. The abovementioned weak QG forcing and less moisture supply plus their resulting weak organization appear to explain why the LRHL MCSs occur less frequently.

As mentioned before, the category distribution of MCSs is closely related to seasonal changes, including increasing surface air temperature from June to August and increasing water vapor transport after the summer monsoon reaches NC. For example, the composite circulation for LRLL MCSs (Fig. 11), occurring mostly in June and early July (Fig. 3b), did show some typical monthly characteristics, namely, with the influences of the subtropical high/summer monsoon mainly on south China. The summer monsoon arrives normally at NC in mid-July, coinciding with the generation of more heavy rainfall events [i.e., more HRLL MCSs to occur in July and most HRHL MCSs to occur in August (Fig. 3)]. Correspondingly, the composite circulations for HRHL

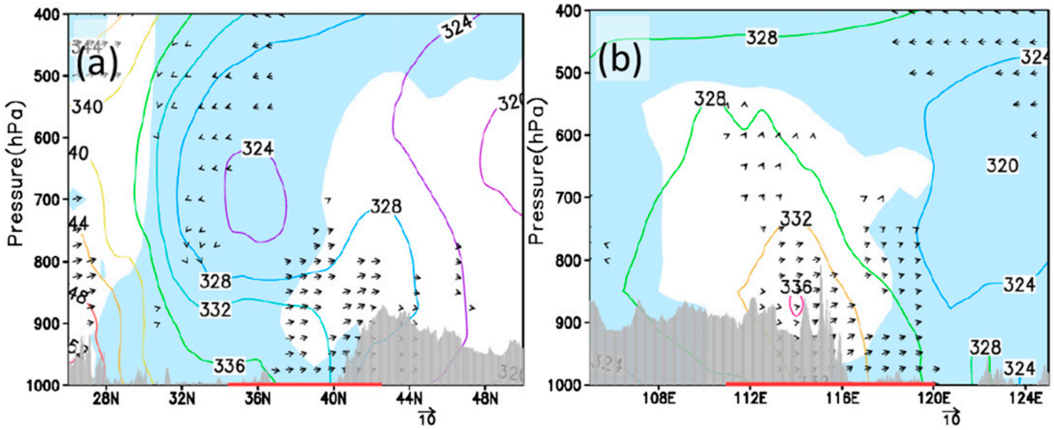

FIG. 12. As in Fig. 8, but for the LRLL events, and they are taken from the south to north along (a) 117°E and (b) from the west to east along 40°N (see Fig. 6d).

and HRLL MCSs show southwesterly flows from south China to the south of NC (see Figs. 7 and 9) and the northwestward extension of the subtropical high, which is consistent with the climatological distribution during the summer season (Ding and Chan 2005).

c. *Environmental thermodynamical parameters*

Figure 13 shows the box-and-whisker plots of the thermodynamical parameters for the four categories of MCSs, while Table 3 lists the statistical significance of their differences. It is evident that the HRHL (LRLL) MCSs had the highest (smallest) mean SBCAPE, MUCAPE, and PW, and the smallest (highest) mean values of LI and CIN. Clearly, these results are qualitatively reasonable because environments with higher (weaker) potential instability and more (less) moisture supply are expected to produce stronger (weaker) updrafts with higher (lower) rainfall rates and (less) CG lightning frequencies. The mean SBCAPE, MUCAPE, and LI of the HRHL MCSs were about twice as much as those of the HRLL MCSs while CIN of the former was about half of that of the latter. MCSs with higher CAPE and lower negative LI tend to produce higher cloud tops because of the larger buoyancy. Generally, the higher the cloud-top height of MCSs, the greater the possibility of forming larger ice particles, which are important for lightning production (Toracinta et al. 1996; Rakov and Uman 2003; Mattos and Machado 2011). In contrast, the HRLL (HRHL) and LRLL (LRHL) MCSs exhibited significant differences in PW, confirming further the important role of moisture supply for the development of heavy rain-producing MCSs.

One may note that the mean SBCAPE for the LRHL MCSs was slightly larger than that of the HRLL MCSs (Fig. 13a). This result appears to be unexpected, but it is attributable to some extent to the former's small sample size. On the other hand, the MUCAPE, which measures better the CAPE than the SBCAPE, shows significant differences in the mean conditional instability between the LRHL and LRLL MCSs, despite the former's small sample size, illustrating the important role of convective instability in CG lightning production. However, given the large range of CAPE for the LRHL MCSs and the different statistical results for the SBCAPE and MUCAPE, the abovementioned differences in CG lightning frequencies may also be attributed to some ice microphysical processes that cannot be derived from the environmental parameters used in the present study. For example, Williams et al. (1989) attributed the generation of intracloud flashes to the accumulation of graupel particles in the central dipole region, and CG lightning to the fallout of ice particles beneath the height of the main negative charge.

4. Summary and conclusions

In this study, we examine the hypothesis that certain environmental conditions determine more or less the relative rainfall amount and CG lightning activity in MCSs that occurred over NC during June–August of 2008–13. A total of 60 MCSs are identified after applying the criterion of a cold cloud region of $\leq -52°C$ that exceeds an area of $\geq 30\,000$ km^2. An analysis of the system-averaged hourly rainfall rate (i.e., R_e) and CG lightning frequency (L_e) in each MCS reveals that the 60 MCSs could be classified into the following four categories: HRHL, HRLL, LRHL, and LRLL with respect to their averaged values of R_e and L_e.

Results show that the MCSs with high convective rainfall rates (i.e., HRHL and HRLL) were most and

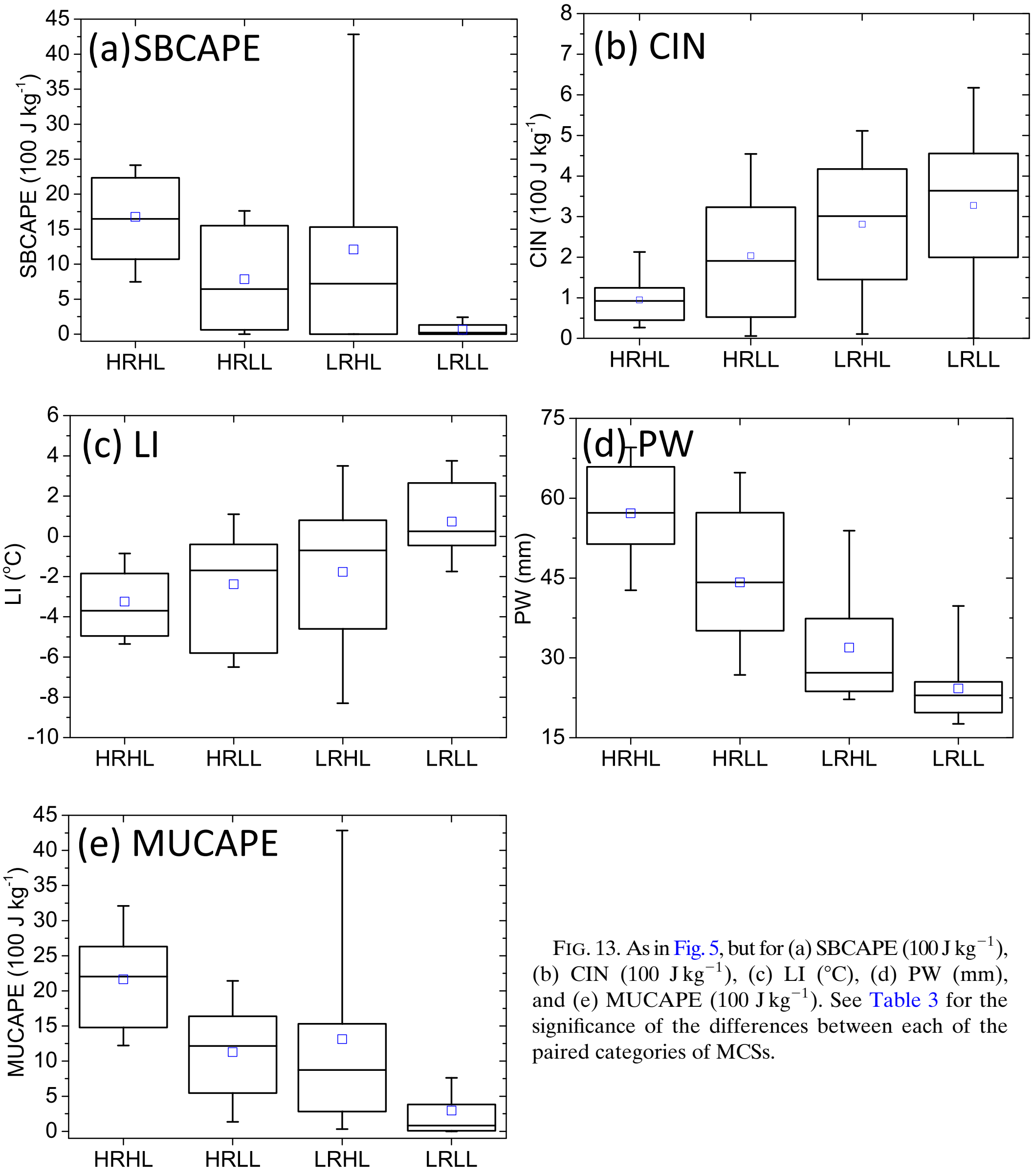

FIG. 13. As in Fig. 5, but for (a) SBCAPE (100 J kg^{-1}), (b) CIN (100 J kg^{-1}), (c) LI (°C), (d) PW (mm), and (e) MUCAPE (100 J kg^{-1}). See Table 3 for the significance of the differences between each of the paired categories of MCSs.

least frequent in July and June, respectively, which coincided with the increased influences of the South China Sea monsoonal flows, whereas the LRHL and LRLL MCSs occurred mostly in June during which the moisture supply was limited. All four categories of events were apt to form (i.e., with their cold cloud top meeting the required size criterion) in the afternoon and the least formed during morning hours. Moreover, the HRHL MCSs could form during any period of a day, while the HRLL MCSs were more frequent during evening hours. Moreover, MCSs with low rainfall rates are likely not prolific in CG lightning production.

Composite analyses of the synoptic-scale circulations and the statistical characteristics of the prestorm thermodynamic parameters show significant differences and similarities in the four categories of MCSs. Both the HRHL and HRLL MCSs occurred in the presence of an upper-level positive divergence anomaly, a midlevel trough, and the lower-tropospheric southwesterly transport of tropical high-θ_{ep} air, giving rise to favorable QG upward motion and the needed moisture supply for heavy rainfall production. Differences between the two corresponding environments include a more intense subtropical high over the west Pacific that favored more northward transport of the high-θ_{ep} air from the South China Sea, and a deeper midlevel trough that assisted in the mesoscale organization of heavy rainfall production associated with the HRHL events. Moreover, the

TABLE 3. The confidence levels of the environmental thermodynamic parameters for each paired category of MCSs at the 0.05 and 0.1 significance levels according to the procedures described in section 2. The letters ''T'' and ''W'' denote two sample *t* tests and a nonparametric Wilcoxon–Mann–Whitney test, respectively. The letter ''X'' denotes the paired two categories of MCSs that are not significantly different from the climatological mean at the 0.1 significance level.

	Pair					
	HRHL	HRHL	HRLL	LRHL	LRHL	LRHL
Index	HRLL	LRLL	LRLL	HRHL	HRLL	LRLL
SBCAPE	T/95%	W/95%	W/95%	W/X	W/X	W/X
MUCAPE	T/95%	W/95%	W/95%	T/90%	T/X	W/95%
CIN	T/95%	T/95%	T/90%	T/X	T/X	T/X
LI	W/X	W/95%	T/95%	W/X	W/X	W/X
PW	T/95%	W/95%	W/95%	T/95%	T/95%	W/X

HRHL MCSs tended to develop in environments with relatively larger surface-based CAPE, most unstable CAPE and PW, and smaller CIN and LI than the HRLL MCSs. In particular, more potentially unstable columns favored the production of more lightning activity in the HRHL MCSs. These favorable synoptic conditions plus intense latent heat release appeared to account for the long duration of the HRHL MCSs (Houze 2004).

As compared to the HRHL and HRLL MCSs, most LRLL events were initiated by topographical lifting with little midtropospheric forcing and much less latent heating, which tended to result in short-lived MCSs. Moreover, the environments with smaller CAPE and PW, and larger CIN and LI favored the development of the LRLL MCSs. In contrast to the LRLL MCSs, the LRHL MCSs exhibited little distinct characteristics from the climatological mean. However, when they are compared in terms of lightning activity, LRHL MCSs showed higher MUCAPE, which was similar to the paired HRHL and HRLL MCSs, illustrating the important role of potentially instability in CG lightning production.

Based on the above results, we may conclude that more favorable mid- to upper-level QG forcing plus ample low-level moisture supply tended to facilitate the development of heavy-rain-producing MCSs, whereas high conditional instability with favorable low-level lifting, accounted more for the generation of MCSs with higher CG lightning frequency. In particular, the results presented herein indicate the importance of seasonal changes in determining the category of MCSs over NC, namely, more LRLL in June, more HRLL in July, and more HRHL in August, as both surface air temperature and monsoonal transport of moisture increase. Nevertheless, despite the environment control of rainfall and lightning to a certain degree, some other processes, such as ice microphysics, may also play an important role in lightning production. It should be mentioned that the above conclusion is derived from limited MCS cases occurring over NC, especially for the small-sample-sized LRHL MCSs. Clearly, more composite studies of thunderstorm events need to be conducted in order to see whether or not the above conclusion is applicable to other MCS events occurring over different geographical locations. Similarly, cloud-resolving modeling studies should be performed to examine the sensitivities of the model-simulated convective rainfall rates and CG lightning frequencies to various environmental parameters mentioned above.

Acknowledgments. We are grateful to Dr. Russ S. Schumacher and three anonymous reviewers for their constructive comments that helped improve the quality of the manuscript. We are also grateful to Dr. Jun Li of the Air Force Meteorological Center of China for his helpful discussion on data processing. This work was supported by the National Basic Research Program of China (973 Program: 2014CB441402) and the National Natural Science Foundation of China (Grant 41205028).

REFERENCES

Anderson, C. J., and R. W. Arritt, 1998: Mesoscale convective complexes and persistent elongated convective systems over the United States during 1992 and 1993. *Mon. Wea. Rev.*, **126**, 578–599, https://doi.org/10.1175/1520-0493(1998)126<0578:MCCAPE>2.0.CO;2.

Bluestein, H. B., and C. R. Parks, 1983: A synoptic and photographic climatology of low-precipitation severe thunderstorms in the southern plains. *Mon. Wea. Rev.*, **111**, 2034–2046, https://doi.org/10.1175/1520-0493(1983)111<2034:ASAPCO>2.0.CO;2.

Carey, L. D., and K. M. Buffalo, 2007: Environmental control of cloud-to-ground lightning polarity in severe storms. *Mon. Wea. Rev.*, **135**, 1327–1353, https://doi.org/10.1175/MWR3361.1.

Chen, M., Y. Wang, F. Gao, and X. Xiao, 2012: Diurnal variations in convective storm activity over contiguous North China during the warm season based on radar mosaic climatology. *J. Geophys. Res.*, **117**, D20115, https://doi.org/10.1029/2012JD018158.

Chen, T. C., S. Y. Wang, W. R. Huang, and M. C. Yen, 2004: Variation of the East Asian summer monsoon rainfall. *J. Climate*, **17**, 744–762, https://doi.org/10.1175/1520-0442(2004)017<0744:VOTEAS>2.0.CO;2.

Cheze, J.-L., and H. Sauvageot, 1997: Area-averaged rainfall and lightning activity. *J. Geophys. Res.*, **102**, 1707–1715, https://doi.org/10.1029/96JD02972.

Colby, F. P., 1984: Convective inhibition as a predictor of convective during AVE-SESAME-2. *Mon. Wea. Rev.*, **112**, 2239–2252, https://doi.org/10.1175/1520-0493(1984)112<2239:CIAAPO>2.0.CO;2.

Cummins, K. L., and M. J. Murphy, 2009: An overview of lightning locating systems: History, techniques, and data uses, with an in-depth look at the U.S. NLDN. *IEEE Trans. Electromagn. Compat.*, **51**, 499–518, https://doi.org/10.1109/TEMC.2009.2023450.

——, ——, E. A. Bardo, W. L. Hiscox, R. B. Pyle, and A. E. Pifer, 1998: A combined TOA/MDF technology upgrade of the U.S. National Lightning Detection Network. *J. Geophys. Res.*, **103**, 9035–9044, https://doi.org/10.1029/98JD00153.

Deierling, W., W. A. Petersen, J. Latham, S. Ellis, and H. J. Christian, 2008: The relationship between lightning activity and ice fluxes in thunderstorms. *J. Geophys. Res.*, **113**, D15210, https://doi.org/10.1029/2007JD009700.

Ding, Y.-H., and J. C. L. Chan, 2005: The East Asian summer monsoon: An overview. *Meteor. Atmos. Phys.*, **89**, 117–142, https://doi.org/10.1007/s00703-005-0125-z.

Doswell, C. A., III, and E. N. Rasmussen, 1994: The effect of neglecting the virtual temperature correction on CAPE calculations. *Wea. Forecasting*, **9**, 625–629, https://doi.org/10.1175/1520-0434(1994)009<0625:TEONTV>2.0.CO;2.

Fritsch, J. M., R. J. Kane, and C. R. Chelius, 1986: The contribution of mesoscale convective weather systems to the warm-season precipitation in the United States. *J. Climate Appl. Meteor.*, **25**, 1333–1345, https://doi.org/10.1175/1520-0450(1986)025<1333:TCOMCW>2.0.CO;2.

Galway, J., 1956: The lifted index as a predictor of latent instability. *Bull. Amer. Meteor. Soc.*, **37**, 528–529.

Goodman, S. J., and D. R. MacGorman, 1986: Cloud-to-ground lightning activity in mesoscale convective complexes. *Mon. Wea. Rev.*, **114**, 2320–2328, https://doi.org/10.1175/1520-0493(1986)114<2320:CTGLAI>2.0.CO;2.

Guo, J., and Coauthors, 2016: Delaying precipitation and lightning by air pollution over the Pearl River Delta. Part I: Observational analyses. *J. Geophys. Res. Atmos.*, **121**, 6472–6488, https://doi.org/10.1002/2015JD023257.

He, H., and F. Zhang, 2010: Diurnal variations of warm-season rainfall over northern China. *Mon. Wea. Rev.*, **138**, 1017–1025, https://doi.org/10.1175/2010MWR3356.1.

Houze, R. A., Jr., 1993: *Cloud Dynamics.* Academic Press, 573 pp.

——, 2004: Mesoscale convective systems. *Rev. Geophys.*, **42**, RG4003, https://doi.org/10.1029/2004RG000150.

Jiang, Z., D.-L. Zhang, R. Xia, and T. Qian, 2017: Diurnal variations of presummer rainfall over Southern China. *J. Climate*, **30**, 755–773, https://doi.org/10.1175/JCLI-D-15-0666.1.

Jin, Y.-Q., N. Lu, and M. Lin, 2010: Advancement of Chinese meteorological Feng–Yun (FY) and oceanic Hai–Yang (HY) satellite remote sensing. *Proc. IEEE*, **98**, 844–861, https://doi.org/10.1109/JPROC.2009.2034283.

Jirak, I. L., W. R. Cotton, and R. L. McAnelly, 2003: Satellite and radar survey of mesoscale convective system development. *Mon. Wea. Rev.*, **131**, 2428–2449, https://doi.org/10.1175/1520-0493(2003)131<2428:SARSOM>2.0.CO;2.

Joyce, R. J., J. E. Janowiak, P. A. Arkin, and P. P. Xie, 2004: CMORPH: A method that produces global precipitation estimates from passive microwave and infrared data at high spatial and temporal resolution. *J. Hydrometeor.*, **5**, 487–503, https://doi.org/10.1175/1525-7541(2004)005<0487:CAMTPG>2.0.CO;2.

Lericos, T. P., H. E. Fuelberg, A. I. Watson, and R. L. Holle, 2002: Warm season lightning distributions over the Florida peninsula as related to synoptic patterns. *Wea. Forecasting*, **17**, 83–98, https://doi.org/10.1175/1520-0434(2002)017<0083:WSLDOT>2.0.CO;2.

Li, H., X. Cui, and D.-L. Zhang, 2017: A statistical analysis of hourly heavy rainfall events over the Beijing metropolitan region during the warm seasons of 2007–2014. *Int. J. Climatol.*, **37**, 4027–4042, https://doi.org/10.1002/joc.4983.

Liu, D., X. Qie, Y. Xiong, and G. Feng, 2011: Evolution of the total lightning activity in a leading-line and trailing stratiform mesoscale convective system over Beijing. *Adv. Atmos. Sci.*, **28**, 866–878, https://doi.org/10.1007/s00376-010-0001-8.

Maddox, R. A., 1980: Meoscale convective complexes. *Bull. Amer. Meteor. Soc.*, **61**, 1374–1387, https://doi.org/10.1175/1520-0477(1980)061<1374:MCC>2.0.CO;2.

Markowski, P., and Y. Richardson, 2010: *Mesoscale Meteorology in Midlatitudes.* Wiley-Blackwell, 424 pp.

Mattos, E. V., and L. A. T. Machado, 2011: Cloud-to-ground lightning and Mesoscale Convective Systems. *Atmos. Res.*, **99**, 377–390, https://doi.org/10.1016/j.atmosres.2010.11.007.

Mazarakis, N., V. Kotroni, K. Lagouvardos, and A. Argiriou, 2008: Storms and lightning activity in Greece during the warm periods of 2003–06. *J. Appl. Meteor. Climatol.*, **47**, 3089–3098, https://doi.org/10.1175/2008JAMC1798.1.

Moncrieff, M., and M. Miller, 1976: The dynamics and simulation of tropical cumulonimbus and squall lines. *Quart. J. Roy. Meteor. Soc.*, **102**, 373–394, https://doi.org/10.1002/qj.49710243208.

Pan, Y., Y. Shen, J. Yu, and P. Zhao, 2012: Analysis of the combined gauge-satellite hourly rainfall over China based on the OI technique. *Acta Meteor. Sin.*, **70**, 1381–1389.

Petersen, W. A., and S. A. Rutledge, 1998: On the relationship between cloud-to-ground lightning and convective rainfall. *J. Geophys. Res.*, **103**, 14 025–14 040, https://doi.org/10.1029/97JD02064.

Rakov, V. A., and M. A. Uman, 2003*: Lightning: Physics and Effects*. Cambridge University Press, 687 pp.

Reap, R. M., 1994: Analysis and prediction of lightning strike distributions associated with synoptic map types over Florida. *Mon. Wea. Rev.*, **122**, 1698–1715, https://doi.org/10.1175/1520-0493(1994)122<1698:AAPOLS>2.0.CO;2.

——, and D. R. MacGorman, 1989: Cloud-to-ground lightning: Climatological characteristics and relationships to model fields, radar observations, and severe local storms. *Mon. Wea. Rev.*, **117**, 518–535, https://doi.org/10.1175/1520-0493(1989)117<0518:CTGLCC>2.0.CO;2.

Ricard, D., V. Ducrocq, and L. Auger, 2012: A climatology of the mesoscale environment associated with heavily precipitating events over a northwestern Mediterranean area. *J. Appl. Meteor. Climatol.*, **51**, 468–488, https://doi.org/10.1175/JAMC-D-11-017.1.

Rudlosky, S. D., and H. E. Fuelberg, 2011: Seasonal, regional, and storm-scale variability of cloud-to-ground lightning characteristics in Florida. *Mon. Wea. Rev.*, **139**, 1826–1843, https://doi.org/10.1175/2010MWR3585.1.

Shen, Y., Y. Pan, and J. Yu, 2013: Quality assessment of hourly merged precipitation product over China (in Chinese). *Trans. Atmos. Sci.*, **36**, 37–46.

——, P. Zhao, Y. Pan, and J. Yu, 2014: A high spatiotemporal gauge - satellite merged precipitation analysis over China. *J. Geophys. Res. Atmos.*, **119**, 3063–3075, https://doi.org/10.1002/2013JD020686.

Sheridan, S. C., J. F. Griffiths, and R. E. Orville, 1997: Warm season cloud-to-ground lightning-precipitation relationships in the south-central United States. *Wea. Forecasting*, **12**, 449–458, https://doi.org/10.1175/1520-0434(1997)012<0449:WSCTGL>2.0.CO;2.

Soriano, L. R., F. De Pablo, and E. G. Díez, 2001: Relationship between convective precipitation and cloud-to-ground lightning in the Iberian Peninsula. *Mon. Wea. Rev.*, **129**, 2998–3003, https://doi.org/10.1175/1520-0493(2001)129<2998:RBCPAC>2.0.CO;2.

Su, Y., L. He, Y. Gong, Z. Li, and Z. Yu, 2011: A study of temporal-spatial distribution and synoptic characteristics of severe convective weather in Beijing, Tianjin and Hebei (in Chinese). *Meteor. Mon.*, **37**, 177–184.

Tao, S., 1980: *Heavy Rainfalls in China* (in Chinese). Science Press, 225 pp.

Tapia, A., J. A. Smith, and M. Dixon, 1998: Estimation of convective rainfall from lightning observations. *J. Appl. Meteor.*, **37**, 1497–1509, https://doi.org/10.1175/1520-0450(1998)037<1497:EOCRFL>2.0.CO;2.

Toracinta, E. R., K. Mohr, E. J. Zipser, and R. E. Orville, 1996: A comparison of WSR-88D reflectivities, SSM/I brightness temperatures, and lightning for mesoscale convective systems in Texas. Part I: Radar reflectivity and lightning. *J. Appl. Meteor.*, **35**, 902–918, https://doi.org/10.1175/1520-0450(1996)035<0902:ACOWRS>2.0.CO;2.

Wilks, D. S., 2011: *Statistical Methods in the Atmospheric Sciences*. Academic Press, 676 pp.

Williams, E. R., M. E. Weber, and R. E. Orville, 1989: The relationship between lightning type and convective state of thunderclouds. *J. Geophys. Res.*, **94**, 13 213–13 220, https://doi.org/10.1029/JD094iD11p13213

Wu, F., X. Cui, D.-L. Zhang, D. Liu, and D. Zheng, 2016: SAFIR-3000 lightning statistics over the Beijing metropolitan region during 2005–07. *J. Appl. Meteor. Climatol.*, **55**, 2613–2633, https://doi.org/10.1175/JAMC-D-16-0030.1.

——, ——, ——, and L. Qiao, 2017: The relationship of lightning activity and short-duration rainfall events during warm seasons over the Beijing metropolitan region. *Atmos. Res.*, **195**, 31–43, https://doi.org/10.1016/j.atmosres.2017.04.032.

Xia, R., D.-L. Zhang, and B. Wang, 2015: A 6-yr cloud-to-ground lightning climatology and its relationship to rainfall over central and eastern China. *J. Appl. Meteor. Climatol.*, **54**, 2443–2460, https://doi.org/10.1175/JAMC-D-15-0029.1.

Xie, P. P., and A. Y. Xiong, 2011: A conceptual model for constructing high-resolution gauge-satellite merged rainfall analyses. *J. Geophys. Res.*, **116**, D21106, https://doi.org/10.1029/2011JD016118.

Xu, W., R. F. Adler, and N.-Y. Wang, 2014: Combining satellite infrared and lightning information to estimate warm - season convective and stratiform rainfall. *J. Appl. Meteor. Climatol.*, **53**, 180–199, https://doi.org/10.1175/JAMC-D-13-069.1.

Yang, X., J. Fei, X. Huang, X. Cheng, L. M. Carvalho, and H. He, 2015: Characteristics of mesoscale convective systems over China and its vicinity using geostationary satellite FY2. *J. Climate*, **28**, 4890–4907, https://doi.org/10.1175/JCLI-D-14-00491.1.

——, J. Sun, and Y. Zheng, 2017: A 5-yr climatology of severe convective wind events over China. *Wea. Forecasting*, **32**, 1289–1299, https://doi.org/10.1175/WAF-D-16-0101.1.

Zhang, D.-L., Y. Lin, P. Zhao, X. Yu, S. Wang, H. Kang, and Y. Ding, 2013: The Beijing extreme rainfall of 21 July 2012: "Right results" but for wrong reasons. *Geophys. Res. Lett.*, **40**, 1426–1431, https://doi.org/10.1002/grl.50304.

Zhang, W., Q. Meng, M. Ma, and Y. Zhang, 2011: Lightning casualties and damages in China from 1997 to 2009. *Nat. Hazards*, **57**, 465–476, https://doi.org/10.1007/s11069-010-9628-0.

Zhong, L., R. Mu, D.-L. Zhang, P. Zhao, Z. Zhang, and N. Wang, 2015: An observational analysis of warm-sector rainfall characteristics associated with the 21 July 2012 Beijing extreme rainfall event. *J. Geophys. Res. Atmos.*, **120**, 3274–3291, https://doi.org/10.1002/2014JD022686.